Keck Observations Confirm a Super-Jupiter Planet Orbiting M Dwarf OGLE-2005-BLG-071L

David P. Bennett[1,2] , Aparna Bhattacharya[1,2], Jean-Philippe Beaulieu[3,4] , Joshua W. Blackman[3] , Aikaterini Vandorou[3] ,
Sean K. Terry[5] , Andrew A. Cole[3] , Calen B. Henderson[6], Naoki Koshimoto[1,2,7] , Jessica R. Lu[8] , Jean Baptiste Marquette[9],
Clément Ranc[1] , and Andrzej Udalski[10]
[1] Code 667, NASA Goddard Space Flight Center, Greenbelt, MD 20771, USA; bennettd@umd.edu
[2] Department of Astronomy, University of Maryland, College Park, MD 20742, USA
[3] School of Physical Sciences, University of Tasmania, Private Bag 37 Hobart, Tasmania 7001 Australia
[4] Institut d'Astrophysique de Paris, 98 bis bd Arago, F-75014 Paris, France
[5] Department of Physics, Catholic University of America, 620 Michigan Avenue, NE Washington, DC 20064, USA
[6] NASA Exoplanet Science Institute, IPAC/Caltech, Pasadena, CA 91125, USA
[7] Department of Astronomy, Graduate School of Science, The University of Tokyo, 7-3-1 Hongo, Bunkyo-ku, Tokyo 113-0033, Japan
[8] University of California Berkeley, Berkeley, CA, USA
[9] Laboratoire d'astrophysique de Bordeaux, Univ. Bordeaux, CNRS, B18N, allée Geoffroy Saint-Hilaire, F-33615 Pessac, France
[10] Warsaw University Observatory, Al. Ujazdowskie 4, 00-478 Warszawa, Poland
Received 2019 September 27; revised 2019 November 25; accepted 2019 December 14; published 2020 January 23

Abstract

We present adaptive optics imaging from the NIRC2 instrument on the Keck II telescope that resolves the exoplanet host (and lens) star as it separates from the brighter source star. These observations yield the K-band brightness of the lens and planetary host star, as well as the lens-source relative proper motion, $\mu_{\rm rel,H}$, in the heliocentric reference frame. The $\mu_{\rm rel,H}$ measurement allows for the determination of the microlensing parallax vector, π_E, which had only a single component determined by the microlensing light curve. The combined measurements of $\mu_{\rm rel,H}$ and K_L provide the masses of the host star, $M_{\rm host} = 0.426 \pm 0.037 M_\odot$, and planet, $m_p = 3.27 \pm 0.32 M_{\rm Jupiter}$ with a projected separation of 3.4 ± 0.5 au. This confirms the tentative conclusion of a previous paper that this super-Jupiter mass planet, OGLE-2005-BLG-071Lb, orbits an M dwarf. Such planets are predicted to be rare by the core accretion theory and have been difficult to find with other methods, but there are two such planets with firm mass measurements from microlensing, and an additional 11 planetary microlens events with host mass estimates $<0.5 M_\odot$ and planet mass estimates >2 Jupiter masses that could be confirmed by high angular follow-up observations. We also point out that OGLE-2005-BLG-071L has separated far enough from its host star that it should be possible to measure the host-star metallicity with spectra from a high angular resolution telescope such as Keck, the Very Large Telescope, the *Hubble Space Telescope*, or the *James Webb Space Telescope*.

Unified Astronomy Thesaurus concepts: Exoplanets (498); Extrasolar gas giants (509); M dwarf stars (982)

1. Introduction

The second exoplanet found by the microlensing method was OGLE-2005-BLG-071Lb, but the discovery paper did not do a detailed analysis of the higher-order microlensing effects that could constrain the masses and distance of the lens system (Udalski et al. 2005). A more detailed analysis was done in a follow-up paper (Dong et al. 2009b) that included high angular resolution *Hubble Space Telescope* (*HST*) observations. Unfortunately, the light curve had no significant signal for finite source effects, the *HST* observations were taken too soon after the event to get a strong measurement of the lens-source relative proper motion, $\mu_{\rm rel}$, and the light curve only constrains one component of the two-dimensional microlensing parallax vector, π_E. However, the light-curve measurements of π_E, $\mu_{\rm rel}$ were marginally inconsistent with each other, and the lack of light-curve finite source effects prevented an additional estimate of the angular Einstein radius. Furthermore, Dong et al. (2009b) pointed out that their estimates of the lens system masses and distance were dependent on the assumption that the excess flux seen at the location of the source in the *HST* images was due to the lens star, rather than a companion to the source. Nevertheless, with the assumption that the excess flux was due to the lens and planetary host star, they conclude that OGLE-

2005-BLG-071Lb may be the most massive planet known to orbit an M dwarf at the time of its publication in 2009.

In this paper, we use adaptive optics observations (AO) with the NIRC2 instrument on the Keck II telescope to identify the lens and planetary host star and provide a precise measurement of the masses and distance of the OGLE-2005-BLG-071L planetary system. These new results largely confirm the more tentative conclusions of Dong et al. (2009b), except for the conclusion that the lens system has thick-disk kinematics. Despite the decade between the publication of Dong et al. (2009b) and this paper, there are still very few known massive planets in wide orbits around low-mass stars. NASA's exoplanet archive[11] lists only 19 planets with masses $>2 M_{\rm Jupiter}$ with semimajor between the snow line (taken to be at $2.7(M/M_\odot)$ au) and 30 au orbiting main-sequence stars with $0.08 M_\odot \leqslant M \leqslant 0.5 M_\odot$. However, two of these are actually planets found by radial velocities with apparent typographical errors in the host masses, so that the correct masses are above $0.5 M_\odot$. The only remaining planet found by radial velocities in this category is GJ 317 b (Johnson et al. 2007), which has host and planet masses of $M_{\rm host} = 0.42 \pm 0.05 M_\odot$ and $m_p = 2.5^{+0.7}_{-0.4} M_{\rm Jupiter}$ with a semimajor axis of

---

[11] https://exoplanetarchive.ipac.caltech.edu/

$a = 1.15 \pm 0.05$ au, based on a combination of radial velocity and astrometric data (Anglada-Escudé et al. 2012). This implies an overlap between the planet's semimajor axis and our estimated snow line position of $d_{\rm snow} = 2.7(M/M_\odot)$ au $= 1.161 \pm 0.135$ au (Kennedy & Kenyon 2008).

The remaining 16 of these wide-orbit planets with super-Jupiter mass planets listed in the NASA Exoplanet Archive have been found by microlensing. These may seem to challenge the core accretion theory expectation that super-Jupiter mass planets should be rare in orbits around low-mass stars (Laughlin et al. 2004), but we must be careful to distinguish between planet and host-star mass measurements and Bayesian mass estimates based on the assumption that all stars are equally likely to host a planet of the measured mass ratio, q. Recent AO image analysis for events MOA-2007-BLG-400 (A. Bhattacharya et al. 2019, in preparation) and MOA-2012-BLG-220 (Vandorou et al. 2019) has indicated host masses much larger than the previous Bayesian analyses suggested, indicating that this prior assumption that all stars are equally likely to host gas giant planets may be flawed. Therefore, it is important to focus on events with mass measurements.

The first microlens exoplanet with a confirmed planet mass of $>2M_{\rm Jupiter}$ orbiting a low-mass star with $0.08M_\odot \leqslant M \leqslant 0.5M_\odot$ was OGLE-2012-BLG-0406 (Poleski et al. 2014), which has host and planet masses of $M_{\rm host} = 0.44 \pm 0.07M_\odot$ and $m_p = 2.73 \pm 0.43M_{\rm Jupiter}$ according to a detailed analysis by Tsapras et al. (2014). In this paper, we present the second such microlens planet, OGLE-2005-BLG-071Lb, with host and planet masses of $M_{\rm host} = 0.431 \pm 0.034M_\odot$ and $m_p = 3.37 \pm 0.30M_{\rm Jupiter}$ at a projected separation of 3.4 ± 0.5 au. However, event OGLE-2005-BLG-071Lb is included in the combined statistical sample of Suzuki et al. (2016), which means that it can readily be included in a statistical analysis of planet properties. In fact, there are three other events from the Suzuki et al. (2016) sample that should allow host and planet mass measurements from high angular resolution follow-up observations. These are OGLE-2008-BLG-355 (Koshimoto et al. 2014), MOA-2009-BLG-387 (Batista et al. 2011), and MOA-2011-BLG-322Lb (Shvartzvald et al. 2014), while such measurements for MOA-2012-BLG-006 (Poleski et al. 2017) in the Suzuki et al. (2016) sample would be quite difficult, because of its bright giant source star. In addition to these events in the Suzuki et al. (2016) sample, the following events are candidates for super-Jupiter planets orbiting low-mass ($<0.5M_\odot$) stars: MOA-2010-BLG-73, OGLE-2013-BLG-0102, OGLE-2013-BLG-1761, OGLE-2015-BLG-0954, MOA-2016-BLG-227, OGLE-2016-BLG-0263, KMT-2016-BLG-1397, and KMT-2017-BLG-1038 (Street et al. 2013; Jung et al. 2015; Shin et al. 2016; Bennett et al. 2017; Hirao et al. 2017; Koshimoto et al. 2017; Zang et al. 2018; Shin et al. 2019). Perhaps the most interesting candidate is OGLE-2018-BLG-1011 (Han et al. 2019), which has two super-Jupiter planets with mass ratios of 0.015 and 0.0095 orbiting a star with an estimated mass of $\sim 0.2M_\odot$.

This paper is organized as follows. In Section 2, we describe the Keck high angular resolution follow-up observations and their analysis, and in Section 3, we discuss the measured lens-source relative proper motion and how it can be used to constrain the microlensing parallax and angular Einstein radius. Our preliminary light-curve modeling is presented in Section 4.

In Section 5, we explain how we constrain the light-curve modeling in order to sample the light curves that are consistent with the data, and then we present the lens system masses, separation, and distance that are implied by the combined light-curve and Keck follow-up data in Section 6. Finally, we discuss the implications of these results and present our conclusions in Section 7.

2. Keck Follow-up Observations and Analysis

We observed the source and lens stars for microlensing event OGLE-2005-BLG-071 with the NIRC2 instrument on the Keck II telescope on 2019 May 28 as a part of our NASA Keck Key Strategic Mission Support (KSMS) program entitled "Development of the WFIRST Exoplanet Mass Measurement Method." The observations were carried out using both the NIRC2 wide and narrow cameras, which employ 1024×1024 pixels with image scales of 39.686 mas/pixel and 9.942 mas/pixel, respectively. All Keck images were taken using the Keck II laser guide star adaptive optics system. The wide images are used for photometric calibrations, and we used a co-add of 8 of 10 dithered, wide camera images in the K_S passband to calibrate reprocessed images from the Vista Variables in the Via Lactea (VVV) survey (Minniti et al. 2010), which is calibrated to the Two Micron All Sky Survey (2MASS; Carpenter 2001) following Beaulieu et al. (2018). (Two of these wide camera images were not used due to relatively poor image quality.) These wide camera images were flat-field and dark current corrected using standard methods. We use Scamp (Bertin 2010a) to perform astrometry on the individual frames. We then did a median stacking using the SWarp package (Bertin et al. 2002; Bertin 2010b).

The details of our methods are described in Batista et al. (2014). We performed aperture photometry on these wide camera images using the latest version of the SExtractor code (Bertin & Arnouts 1996). These wide images were used to detect and match as many bright isolated stars as possible to our custom reduction (Beaulieu et al. 2016) of the calibrated VVV images. Once the wide camera images were calibrated, we calibrated the narrow camera images to the wide camera images. This procedure provided an overall calibration precision for the co-added narrow camera image based on nominal uncertainties of 0.06 magnitudes. SExtractor, Scamp, and SWarp are distributed by astromatic.net (Bertin et al. 2012).

We took 40 dithered NIRC2 narrow camera images, which were taken on the same night as the wide camera images, and the 23 best images were combined to make the image shown in Figures 1(a) and (b) after correcting for achromatic differential refraction (Yelda et al. 2010) and geometric distortion (Service et al. 2016). Chromatic differential refraction is negligible compared to our measurement uncertainties (Gubler & Tytler 1998), so we ignore it. The point-spread function (PSF) FWHM of this image is ≈ 65 mas. Because the source and candidate lens stars are separated by ~ 1 FWHM, we must analyze the Keck data with a PSF fitting code to measure the astrometry and photometry of this two-star system. Following Bhattacharya et al. (2018), we use DAOPHOT (Stetson 1987) for this analysis, which has a proven ability to handle peculiar PSF shapes that are sometimes encountered in adaptive optics images (Bennett et al. 2010). The initial DAOPHOT reduction did not detect the fainter component of the source plus lens star blend because it does not try to find stars at such small
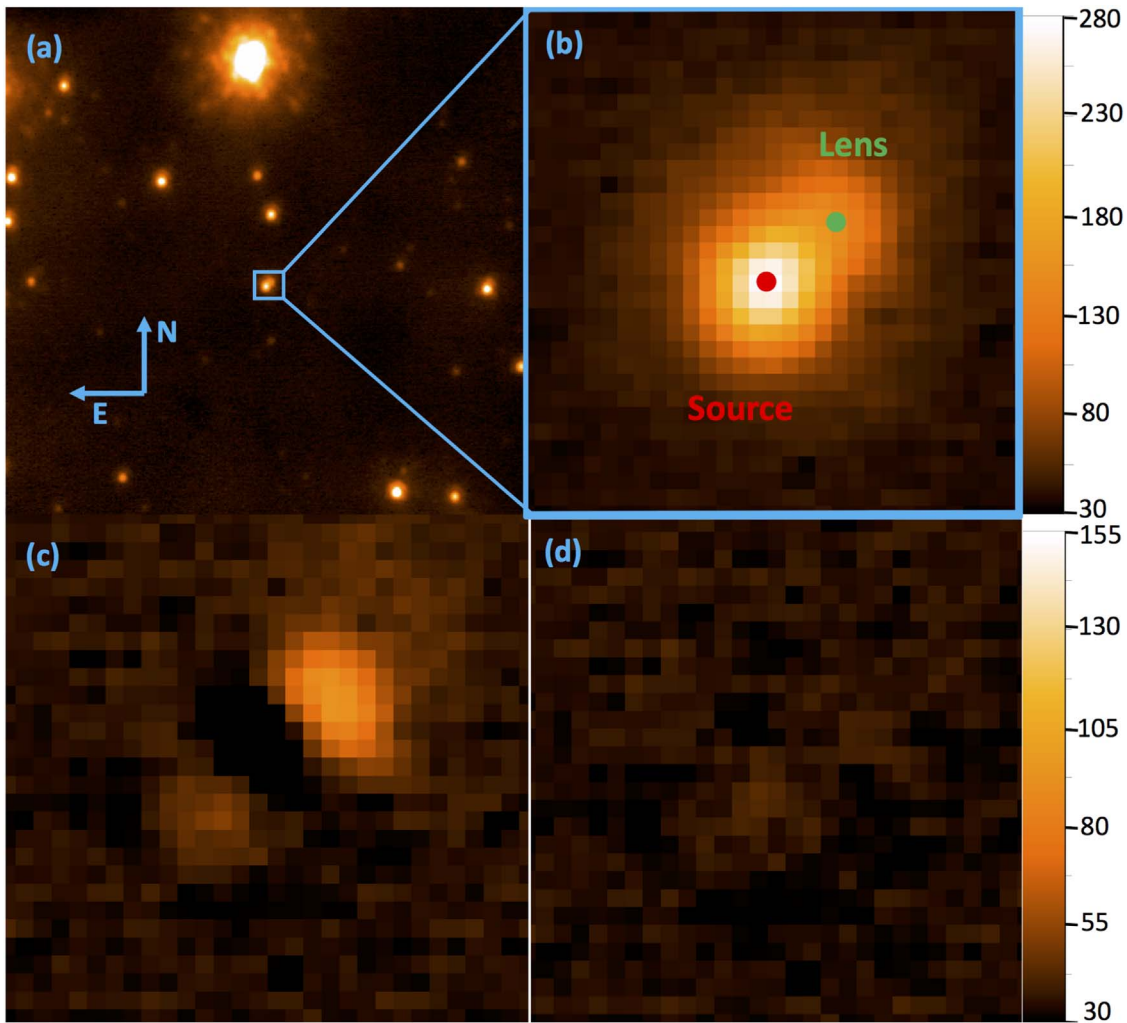
Figure 1. (a) The co-added sum of 23 Keck-NIRC2 narrow camera images with an exposure of 60 s, and (b) a closeup of the OGLE-2005-BLG-071 source and lens stars on the right. The lens star is located 41.5 ± 1.3 mas west and 36.1 ± 1.3 mas north of the source star. Panel (c) is the residual image from a DAOPHOT single-star fit, and (d) is the residual image from a two-star fit. The color bar on the top right refers to panels (a) and (b), and the color bar on the bottom right refers to both panels (c) and (d).

separations. This resulted in the residual image shown in Figure 1(c) when the best-fit PSF model was subtracted from the the original image (shown in Figures 1(a) and (b)). Following Bhattacharya et al. (2018), we then added an additional source at the position of the brightest residual in Figure 1(c) and reran DAOPHOT. This resulted in the two stars indicated in Figure 1(b) and the two-star fit residual shown in Figure 1(d). This two-star fit residual is nearly featureless, indicating that the Keck image is well modeled by two stars separated by ~ 1 FWHM. This analysis reveals that the magnitudes of the two stars are $K_S = 17.679 \pm 0.060$ and $K_L = 18.925 \pm 0.062$, where the uncertainty is dominated by the calibration uncertainty. The identification of the brighter star as the source star is determined from the predicted K-band brightness of the source star.

In order to determine which star is the source and which is the candidate lens star, we need to compare to the light-curve predictions. The Dong et al. (2009b) paper gives magnitudes and colors based on an early version of the OGLE-III survey calibrations and uses old values for the intrinsic color and magnitude of red clump giant stars to estimate the extinction. We redo this analysis with updated OGLE-III light curves, with the final instrumental magnitudes, the final OGLE-III

magnitude and color calibrations (Szymański et al. 2011), and the Nataf et al. (2013) values for the properties of the bulge red clump giant stars at the Galactic position ($l = -4°.4198$, $b = -3°.7864$) of the target. Using standard methods (Bennett et al. 2010), we find the centroid of the red clump for stars within $2'$ of the source to be $[(V - I)_{\rm rcg}, I_{\rm rcg}] = [1.85, 15.71]$. Based on the intrinsic red clump giant stars from Nataf et al. (2013), this gives a color excess of $E(V - I) = 0.79$ and I-band extinction of $A_I = 1.10$, which together imply a V-band extinction of $A_V = 1.89$. The K-band extinction was determined to be $A_K = 0.15 \pm 0.05$ from the online VVV extinction calculator (Gonzalez et al. 2011) using the Nishiyama et al. (2009) extinction law. From the best-fit constrained light-curve model, described in Section 5, we find a source color of $V_S - I_S = 1.43$, so the extinction corrected color is $V_{S0} - I_{S0} = 0.64$. Using the color–color relations of Kenyon & Hartmann (1995) and the I-band magnitude, $I_S = 19.54$ from this same model, we predict a source magnitude of $K_S = 17.89$. This can only be consistent with the brighter of the two blended stars shown in Figures 1(a) and (b). The fit source brightness is fainter than the brighter star by about 3σ, which suggests that the source might have a faint companion.

3. The Lens–Source Relative Proper Motion

The measured offset of the lens star with respect to the source is ΔR.A. $= -41.5 \pm 1.3$ mas and Δdecl.$=36.1 \pm 1.3$ mas. The Keck observations were taken on 2019 May 28, which was 14.103 yr after the event. The apparent relative motion of the lens and source is primarily due to their space motions, but there is also a contribution from parallax due to the orbital motion of the Earth. However, this contribution is $\lesssim 0.2$ mas for a lens more distant that $D_L \gtrsim 2$ kpc. We can ignore this contribution, because it is much smaller than the error bars on our position measurements, so the lens-source relative proper motion is

$$
\begin{aligned}
\boldsymbol{\mu}_{\mathrm{rel,H}} &= (\mu_{\mathrm{rel,H,E}},\ \mu_{\mathrm{rel,H,N}}) \\
&= (-2.945 \pm 0.091,\ 2.563 \pm 0.091)\,\mathrm{mas\ yr^{-1}}, \quad (1)
\end{aligned}
$$

where the subscript H indicates that this is the proper motion in the heliocentric reference frame, while the E and N subscripts indicate the east and north directions. We can also convert these relative proper motions to the Galactic coordinates:

$$
\begin{aligned}
\boldsymbol{\mu}_{\mathrm{rel,H}} &= (\mu_{\mathrm{rel,H,}l},\ \mu_{\mathrm{rel,H,}b}) \\
&= (0.703 \pm 0.091,\ 3.840 \pm 0.091)\,\mathrm{mas\ yr^{-1}}. \quad (2)
\end{aligned}
$$

The uncertainties in the separation measurements were calculated following King (1983), using the equation

$$
\sigma_x = 0.65238 \times \mathrm{FWHM} \times \sqrt{\tfrac{4}{3}} \times \frac{\sigma_{\mathrm{F}}}{\mathrm{F}} \quad (3)
$$

where F is the flux of the star with the measured position.

3.1. Source and Lens Proper Motion

In addition to the lens-source relative proper motion, we can also compare the astrometry of our 2019 Keck images to the astrometry of the *HST* images taken in 2005 and 2006 (Dong et al. 2009b). We select the 2005 *V*-band (F555W) images taken 14.013 yr before the Keck images because these will provide a negligible parallax signal while providing a precise position for source star, since the lens-source separation is quite small one month after the event peak, and the source was still magnified by a factor of ~ 2 and is much brighter than the lens in the *V* band. The *HST* data was reduced with DOLPHOT (Dolphin 2000), which does not produce astrometry with precision that is quite as high as the method of Anderson & King (2000, 2004, 2006), but this will have little influence on the final proper motion results, because the uncertainties are dominated by the uncertainties in the *Gaia* astrometry.

There are three relatively bright stars within 5″ of the OGLE-2005-BLG-071 microlensing event with proper motion measurements in the *Gaia* DR2 data release (*Gaia* Collaboration et al. 2018a). These stars have *Gaia* numbers 4041487538966873216, 4041487538966873344, and 4041487538966886016, and all three of these events have reliable proper motion measurements as evidenced by their renormalized unit weight error values of <1.3 (Lindegren 2018). Their *V*-band magnitudes are 18.399, 18.238, and 16.953, respectively. This allows us to determine the source proper motions in Galactic coordinates:

$$
\boldsymbol{\mu}_S = (\mu_{S,l},\ \mu_{S,b}) = (-4.99 \pm 0.19,\ -0.69 \pm 0.25)\,\mathrm{mas\ yr^{-1}}. \quad (4)
$$

We can then add $\boldsymbol{\mu}_S$ and $\boldsymbol{\mu}_{\mathrm{rel,H}}$ from Equation (2) to determine the lens proper motion,

$$
\boldsymbol{\mu}_L = (\mu_{L,l},\ \mu_{L,b}) = (-3.14 \pm 0.21,\ 3.38 \pm 0.27)\,\mathrm{mas\ yr^{-1}}. \quad (5)
$$

The source proper motion, $\boldsymbol{\mu}_S$, is dominated by the reflex motion of Galactic rotation and is quite typical for the proper motion of Galactic bulge star. Dong et al. (2009b) claimed that the OGLE-2005-BLG-071L lens star had the kinematics of a thick-disk star. If true, this would be a surprise because super-Jupiter mass planets are thought to form preferentially around more massive, high metallicity stars. Thick disk stars tend to have low metallicity, so it would be surprising if OGLE-2005-BLG-071Lb was a super-Jupiter mass planet orbiting a a low-mass, low metallicity star. The Dong et al. (2009b) claim of thick-disk kinematics is based upon their claim of velocity with respect to the local standard of rest of $v_{\mathrm{LSR}} = 103 \pm 15\,\mathrm{km\,s^{-1}}$. We can compare this to our measurement of the lens star transverse velocity if we assume a lens distance of $D_L = 3.5$ kpc, which is the favored D_L according to the analysis presented below in Section 6. We find a transverse velocity of $\boldsymbol{v}_L = (v_{L,ll}, v_{L,b}) = (-52.5, 56.5)$ $\mathrm{km\,s^{-1}}$ for a total transverse velocity of $77\,\mathrm{km\,s^{-1}}$. This is within 2σ of the Dong et al. (2009b) v_{LSR}, but in fact, Dong et al. (2009b) do not specify that their v_{LSR} value refers to a transverse velocity, so it is probably supposed to be a full three-dimensional velocity, with the unmeasured radial component just an estimate from averaging over a Galactic model. This would imply that their v_{LSR} value is probably consistent with our measured $77\,\mathrm{km\,s^{-1}}$ transverse velocity. However, their conclusion that the OGLE-2005-BLG-071L has thick-disk kinematics does not follow.

The *Gaia* DR2 data release enables a much more accurate test of the kinematic properties for stars that are a few kiloparsecs from the Sun. In particular, the Gaia Collaboration et al. (2018b) study of the Milky Way disk kinematics provides valuable information on the kinematic properties of stars in the vicinity of OGLE-2005-BLG-071L, located at a distance of $D_L \sim 3.5$ kpc toward the Galactic bulge at ~ 0.22 kpc below the Galactic plane. Figure 11 of Gaia Collaboration et al. (2018b) indicates that the median orbital velocity in the disk has dropped to $v_\phi = 205\,\mathrm{km\,s^{-1}}$ compared to $v_\phi = 240\,\mathrm{km\,s^{-1}}$ at the solar circle. This means that the velocity of OGLE-2005-BLG-071L compared to the stars in its vicinity is $v_{L,\mathrm{VSR}} = (-17.5, 56.5)\,\mathrm{km\,s^{-1}}$ (where VSR stands for vicinity standard of rest). The median stellar velocity in the z direction (perpendicular to the Galactic disk) does not differ from the median velocity of 0 at the solar circle, but the velocity dispersions in both directions grow to $\sigma_{v_\phi} = 45\,\mathrm{km\,s^{-1}}$ and $\sigma_{v_z} = 38\,\mathrm{km\,s^{-1}}$. Thus, the l and b components of $\boldsymbol{v}_L$ are 0.4σ and 1.5σ from the center of the velocity distribution. So, we conclude that OGLE-2005-BLG-071L has normal stellar kinematics for a star at its location, and it should not be considered to be a thick-disk star.

3.2. Geocentric Relative Proper Motion

Our light-curve modeling is done in a geocentric reference frame that differs from the heliocentric frame by the instantaneous velocity of the Earth at the time of peak magnification. This avoids large corrected uncertainties for the light-curve parameters that would be quite common for

Table 1
Best-fit Model Parameters Unconstrained by Keck or *HST* Observations

| Parameter | $u_0 < 0$ | | $u_0 > 0$ | | MCMC Averages |
	$s < 1$	$s > 1$	$s < 1$	$s > 1$	
t_E (days)	77.100	70.942	72.324	69.825	71.8 ± 3.2
t_0 (HJD$'$)	3480.7048	3480.7048	3480.6971	3480.6971	3480.702 ± 0.004
u_0	-0.021476	-0.027294	0.027680	0.023016	0.006 ± 0.025
s	0.75384	1.29784	0.75805	1.29140	1.15 ± 0.24
α (rad)	-1.65212	-1.64712	1.65041	1.64547	-0.40 ± 1.60
$q \times 10^3$	6.5824	7.1689	6.8499	7.1594	6.98 ± 0.29
t_* (days)	0.01026	0.01652	0.02106	0.03092	0.018 ± 0.012
$\pi_{E,N}$	-0.9150	-0.6331	0.08204	-0.1065	-0.42 ± 0.41
$\pi_{E,E}$	-0.3692	-0.3058	-0.21894	-0.2311	-0.279 ± 0.066
fit χ^2	1241.91	1226.24	1250.50	1231.14	
dof	1271	1271	1271	1271	

models done in the heliocentric frame. However, this also means that the lens-source relative proper motion that we measure with follow-up observations is not in the same reference frame as the light-curve parameters. This is an important issue because, as we show below, the measured relative proper motion can be combined with the microlensing parallax light-curve parameter to determine the mass of the lens system. The relation between the relative proper motions in the heliocentric and geocentric coordinate systems are given by (Dong et al. 2009b)

$$\boldsymbol{\mu}_{\mathrm{rel,H}} = \boldsymbol{\mu}_{\mathrm{rel,G}} + \frac{\boldsymbol{v}_\oplus \pi_{\mathrm{rel}}}{\mathrm{au}}, \qquad (6)$$

where $\boldsymbol{v}_\oplus$ is the projected velocity of the Earth relative to the Sun (perpendicular to the line of sight) at the time of peak magnification. The projected velocity for OGLE-2005-BLG-071 is $\boldsymbol{v}_{\oplus E,N} = (15.508, 4.685)$ km s^{-1} = $(3.271, 0.988)$ au/yr at the peak of the microlensing light curve, HJD$'$ = 3480.70. The relative parallax is defined as $\pi_{\mathrm{rel}} \equiv 1/D_L - 1/D_S$, where D_L and D_S are lens and source distances, so Equation (6) can be written as

$$\boldsymbol{\mu}_{\mathrm{rel,G}} = \boldsymbol{\mu}_{\mathrm{rel,H}} - (3.271, 0.988) \times (1/D_L - 1/D_S),$$

which is a more convenient form since $\boldsymbol{\mu}_{\mathrm{rel,H}}$ has been measured directly from the Keck images. Now at each possible lens distance, we can use the $\boldsymbol{\mu}_{\mathrm{rel,G}}$ value from Equation (6) to determine the angular Einstein radius, $\theta_E = \mu_{\mathrm{rel,G}} t_E$. As we explain below, the $\boldsymbol{\mu}_{\mathrm{rel,G}}$ can also be used to convert a one-dimensional microlensing parallax measurement into a full measurement of the microlensing parallax vector. The lens flux and $\boldsymbol{\mu}_{\mathrm{rel,H}}$ measurements from the Keck observations and the one-dimensional parallax measurement constrain the angular Einstein radius, the microlensing parallax vector and, therefore, the mass and distance of the lens.

4. Light Curve Model

Dong et al. (2009b) present a detailed discussion of light-curve models for OGLE-2005-BLG-071, and we have little to add to this discussion. However, we find it necessary to do our own modeling of this event in order to apply the constraints from our Keck observations in a Markov Chain Monte Carlo (MCMC) analysis. We use the same data set as Dong et al. (2009b) with some minor modifications. First, we drop the Palomar data set because it covers only 80 minutes when the

magnification changes by less than 5%. Because the source and background fluxes are fit independently for each data set (Rhie et al. 1999), the Palomar data do not provide a significant constraint on the light-curve model. As is common practice (Dong et al. 2009b), once we have established all the possible degenerate solutions, we renormalize the χ^2 per degree of freedom to be $\chi^2/\mathrm{dof} \simeq 1$ in order to obtain more reasonable error bars on the inferred parameters of the lens system.

Table 1 shows the parameters of our four degenerate light-curve models and the MCMC average of all four models. The parameters that apply to single lens models are the Einstein radius crossing time, t_E, the time of closest alignment between the source and the lens system center of mass, t_0, and the distance of closest approach between the source and the lens system center of mass, u_0, which is given in units of the Einstein radius. The addition of a second lens mass requires three additional parameters, the mass ratio of the two lens masses, q, their separation, s, in units of the Einstein radius, and angle, α, between the source trajectory and the transverse line that passes through the two lens masses. In addition, a large fraction of binary lens systems exhibit finite source effects that can be modeled with the addition of the source radius crossing time parameter, t_*. For high magnification events, like OGLE-2005-BLG-071, the transformation $s \rightarrow 1/s$ often has only a slight change on the shape of the light curve. This is known as the close–wide degeneracy, and it applies to OGLE-2005-BLG-071 (Udalski et al. 2005; Dong et al. 2009b).

Many longer duration binary lens events, like OGLE-2005-BLG-071, exhibit light-curve effects due to the orbital motion of the Earth during the event. This is known as the microlensing parallax effect, and Dong et al. (2009b) have shown that OGLE-2005-BLG-071 has a significant signal, which is described by a two-dimensional vector, $\boldsymbol{\pi}_E$, that is parallel to the direction of lens-source relative motion. The inclusion of the microlensing parallax parameters introduces an addition degeneracy. Without microlensing parallax, the transformation $u_0 \rightarrow -u_0$, $\alpha \rightarrow -\alpha$ produces exactly the same light curve, and it can just be thought of as a change of parameters. When microlensing parallax is added, however, this transformation amounts to a reflection of the lens system orientation with respect to the orbit of the Earth, so it is no longer a trivial, exact degeneracy (unless the lens system lies in the ecliptic plane). This second degeneracy is often referred to as the $u_0 \leftrightarrow -u_0$ degeneracy. We do not include lens orbital motion for these unconstrained models, which we consider only to offer a comparison to the models with models with the
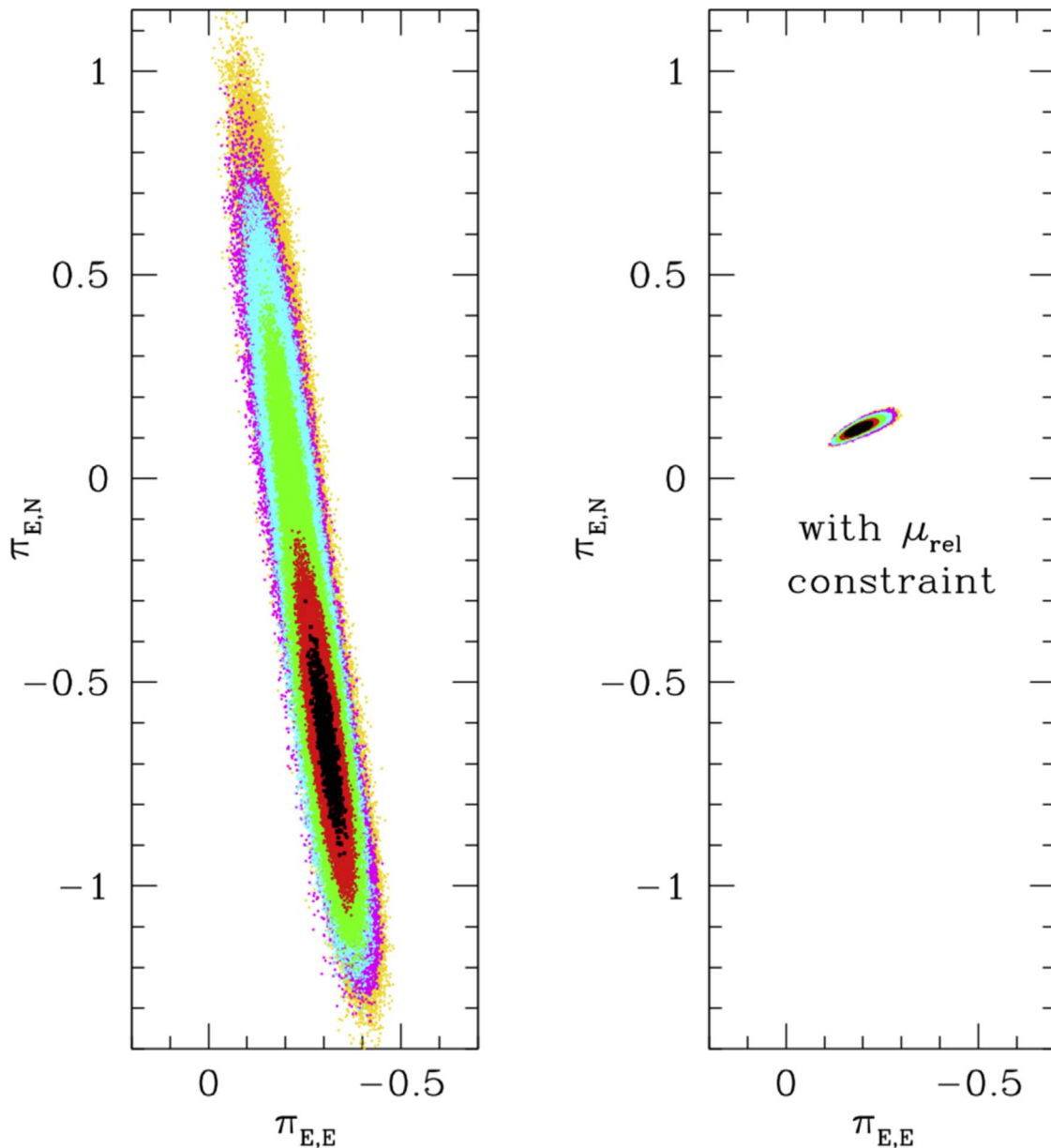
Figure 2. Left panel: the π_E distribution from light-curve modeling without any constraints from follow-up observations. Right panel: the π_E distribution resulting from the addition of the high resolution follow-up imaging constraints. The following color scheme is used to denote the χ^2 differences from the best-fit light-curve model: black represents $\Delta\chi^2 < 1$, red represents $\Delta\chi^2 < 4$, green represents $\Delta\chi^2 < 16$, cyan represents $\Delta\chi^2 < 25$, and magenta represents $\Delta\chi^2 \geqslant 25$. (The weighting of the models does not depend on the $\Delta\chi^2$ values, however.) The right panel shows that the Keck relative proper motion measurements constrain the north component of π_E ($\pi_{E,N}$), which was largely unconstrained by the light curve. Without the $\boldsymbol{\mu}_{\rm rel,H}$ measurement, in the left panel, the light curve slightly favors solutions with $\pi_{E,N} < 0$, but the constraint forces $\pi_{E,N} > 0$. Note that this figure combines both the degenerate $u_0 > 0$ and $u_0 < 0$ models.

constraints from high angular resolution follow-up observations.

There is one fixed parameter not included in Table 1. The geocentric coordinate system used to define the microlensing parallax parameters is fixed to the Earth's orbital velocity at $t_{\rm fix} = 3480.7$. These unconstrained models have 1298 observations, 9 nonlinear parameters, and 18 linear parameters for a total of 1271 degrees of freedom.

5. Relative Proper Motion Constraints on π_E and Light-curve Models

As Figure 2 indicates, the microlensing light curve provides a fairly tight constraint on one component of the microlensing

parallax vector, π_E. This is the component in the direction of the Earth's acceleration, which is nearly parallel to the east–west direction. But as it is often the case (Muraki et al. 2011), only the $\pi_{E,E}$ component of the microlensing parallax vector is measured precisely. As shown in the left panel of Figure 2, the 2σ range for $\pi_{E,N}$ is $-0.39 < \pi_{E,N} < 0.43$. However, the microlensing parallax vector, π_E, is parallel to the $\boldsymbol{\mu}_{\rm rel,G}$ vector, and the two quantities are related by

$$\pi_E = \frac{\pi_{\rm rel}}{t_E} \frac{\boldsymbol{\mu}_{\rm rel,G}}{|\mu_{\rm rel,G}|^2}, \qquad (7)$$

so with measurements of $\pi_{E,E}$ and $\boldsymbol{\mu}_{\rm rel,H}$, we can use Equations (6) and (7) to solve for $\pi_{E,N}$ (Gould et al. 1994;

Table 2
Best-fit Model Parameters with $\mu_{\rm rel,H}$ and Magnitude Constraints

| Parameter | $u_0 < 0$ | | $u_0 > 0$ | | MCMC Averages |
	$s < 1$	$s > 1$	$s < 1$	$s > 1$	
t_E (days)	68.357	68.221	68.420	67.912	68.1 ± 1.2
t_0 (HJD$'$)	3480.6751	3480.6919	3480.6755	3480.6922	3480.692 ± 0.007
u_0	-0.024468	-0.028289	0.024401	0.028439	0.001 ± 0.028
s_0	0.76151	1.28821	0.76067	1.28956	1.233 ± 0.163
α (rad)	-1.64182	-1.64233	1.64218	1.64267	0.06 ± 1.64
$q \times 10^3$	7.0943	7.2753	7.1262	7.3421	7.32 ± 0.16
t_* (days)	0.05103	0.05113	0.05087	0.05143	0.0513 ± 0.0014
$\pi_{\rm E,N}$	0.1223	0.1234	0.1218	0.1204	0.123 ± 0.010
$\pi_{\rm E,E}$	-0.1899	-0.1913	-0.1685	-0.1909	-0.192 ± 0.021
$\dot{s}_x$ (days^{-1})	0.00139	-0.00126	0.00139	-0.00128	-0.00081 ± 0.00084
$\dot{s}_y$ (days^{-1})	-0.00187	-0.00128	0.00173	0.00102	-0.00002 ± 0.00081
I_s	19.550	19.543	19.554	19.539	19.542 ± 0.026
V_s	20.981	20.975	20.971	20.986	20.974 ± 0.026
fit χ^2	1234.29	1230.13	1234.27	1229.98	
dof	~ 1273	~ 1273	~ 1273	~ 1273	

Ghosh et al. 2004; Bennett et al. 2007). While this leads to a quadratic equation (Gould 2014), only one of these solutions has a positive lens distance, D_L. Bhattacharya et al. (2018) have argued that the odds of an ambiguity due the two solutions of this quadratic equation are negligible, because even is cases where both solutions have positive D_L, they predict very different lens magnitudes.

The volume of the light-curve model parameter space that is allowed by the Keck observation constraints on $\mu_{\rm rel,H}$ and K_L is very much smaller than the volume allowed without those constraints as Figure 2 indicates. As a result, we would have poor sampling of the posterior distributions if we were to apply these constraints to Markov Chains. So, following Bhattacharya et al. (2018) we implement constraints on $\mu_{\rm rel,H}$ and K_L during the light-curve modeling. The relative proper motion, $\mu_{\rm rel,H}$, is constrained by the measurement given in Equation (1), and we constrain the lens star K-band brightness to be $K_L = 18.925 \pm 0.062$, as discussed in Section 2. Following Bhattacharya et al. (2018), these constraints implement a χ^2 contribution from each of the constraints and add it to the light-curve fit χ^2 inside the modeling code (Bennett 2010). We use the empirical mass–luminosity relation described by Bennett et al. (2018), which is a combination of several different mass–luminosity relations for different mass ranges. For $M_L \geqslant 0.66\,M_\odot$, $0.54\,M_\odot \geqslant M_L \geqslant 0.12\,M_\odot$, and $0.10\,M_\odot \geqslant M_L \geqslant 0.07\,M_\odot$, we use the relations of Henry & McCarthy (1993), Delfosse et al. (2000), and Henry et al. (1999), respectively. In between these mass ranges, we linearly interpolate between the two relations used on the boundaries. That is, we interpolate between the Henry & McCarthy (1993) and the Delfosse et al. (2000) relations for $0.66\,M_\odot > M_L > 0.54\,M_\odot$, and we interpolate between the Delfosse et al. (2000) and Henry et al. (1999) relations for $0.12\,M_\odot > M_L > 0.10\,M_\odot$.

For the mass–luminosity relations, we must also consider the foreground extinction. At a Galactic latitude of $b = -3\overset{\circ}{.}7865$, and a lens distance of ~ 2 kpc, the lens system is likely to be behind some, but not all, of the dust that is in the foreground of the source. We assume a dust scale height of $h_{\rm dust} = 0.10 \pm 0.02$ kpc, so that the extinction in the

foreground of the lens is given by

$$A_{i,L} = \frac{1 - e^{-|D_L(\sin b)/h_{\rm dust}|}}{1 - e^{-|D_S(\sin b)/h_{\rm dust}|}} A_{i,S}, \qquad (8)$$

where the index i refers to the passband: I, V, or K. In the Markov Chain calculations themselves, we fix $D_S = 8.8$ kpc for our source star at a Galactic longitude of $l = -4\overset{\circ}{.}4198$, and we fix the dust scale height at $h_{\rm dust} = 0.10$ kpc. (The distance to Galactic bar at this longitude is 8.8 kpc; Nataf et al. 2013). But, we remove this distance restriction by reweighting the links in the Markov Chain when we sum them for our final results as discussed in Section 6.

In addition to these constraints, we also include two additional parameters to describe the orbital motion of the planet. Unlike the case of the two planet event OGLE-2006-BLG-109 (Gaudi et al. 2008; Bennett et al. 2010), the light curve does not provide significant constraints on the planetary orbital motion, although we fix the orbital period at 5000 days to avoid the possibility of an unphysical future encounter between the source and lens system that might occur if we assumed constant velocities. The two orbital motion parameters are $\dot{s}_x$ and $\dot{s}_y$, which are the orbital motion in the direction of star–planet separation (at $t = t_{\rm fix}$) and the perpendicular direction, respectively. As in the case of MOA-2009-BLG-266 (Muraki et al. 2011), the inclusion of orbital motion does affect the relative weighting of the degenerate models. In particular, the inclusion of orbital motion substantially decreases the χ^2 difference between the wide and close models, which are only disfavored by $\Delta\chi^2 \approx 4.3$ for the constrained models. This can be seen by a comparison of the χ^2 difference between the wide and close models for the constrained model, shown in Table 2, and the unconstrained models without orbital motion, shown in Table 1. As was the case with MOA-2009-BLG-266, the χ^2 difference between the $u_0 > 0$ and $u_0 < 0$ solutions is also decreased. The best-fit constrained light curve is shown in Figure 3. Despite the two additional light-curve parameters, the model constraints on the relative proper motion and lens magnitude increase the number of degrees of freedom to 1272 or 1274, depending on whether the upper limits on the combined lens plus source V and I magnitudes are counted as full constraints.
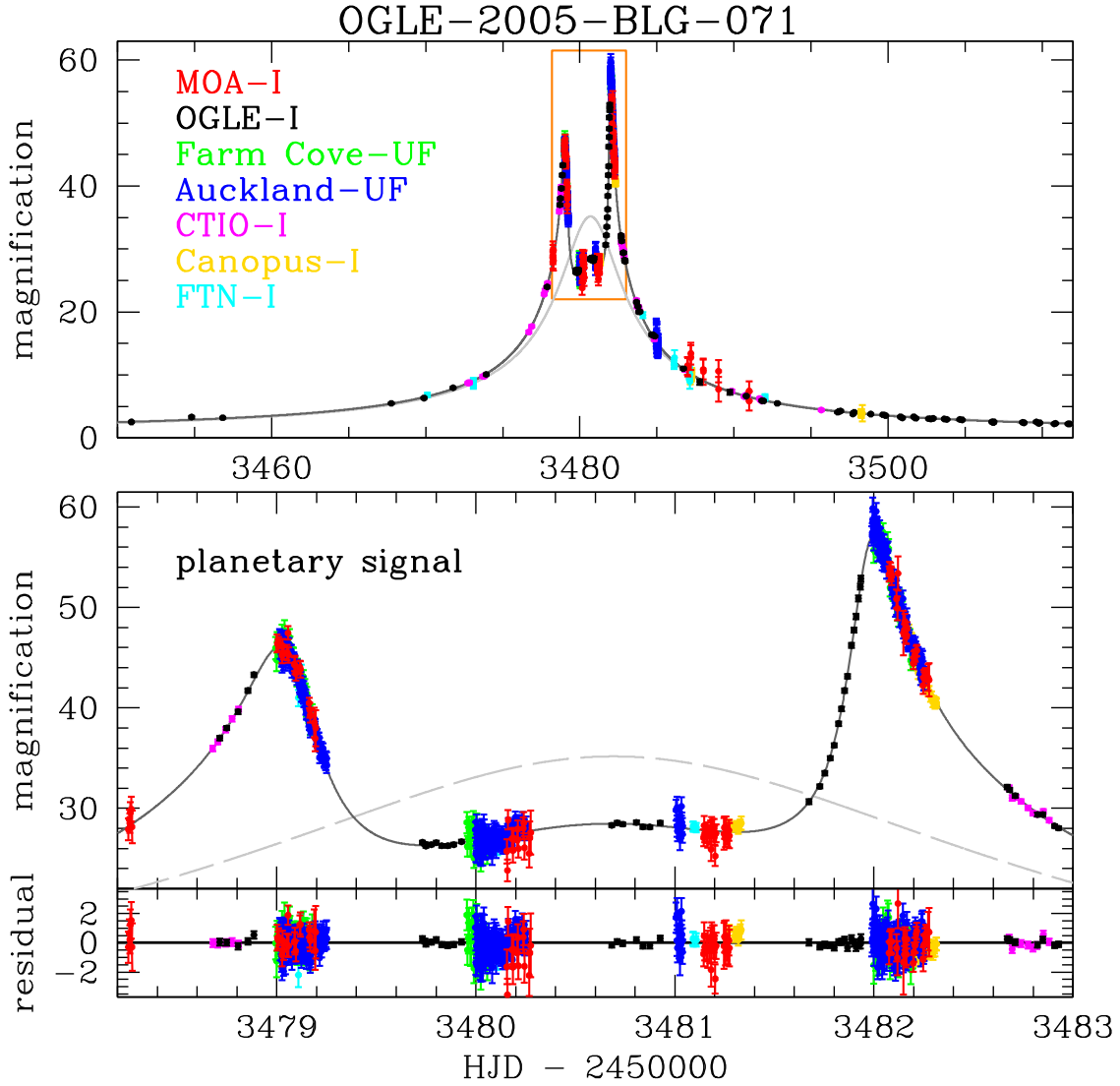
Figure 3. Best-fit light curve with the constraints on the relative proper motion, $\mu_{\rm rel,H}$, and host-star magnitude, K_L, constraints. This is the model from the fifth column of Table 2, with $u_0 > 0$ and $s > 1$.

While these constraints have little effect on the best-fit model χ^2, they have a dramatic effect on the allowed range of microlensing parallax parameters, as Figure 2 indicates. The 2σ range for $\pi_{E,N}$ is reduced from $-1.07 < \pi_{E,N} < 0.49$ to $0.104 < \pi_{E,N} < 0.144$, which is a reduction of a factor of 39 in uncertainty. This yields a microlensing parallax amplitude of $\pi_E = 0.229 \pm 0.023$, which will be used in Section 6 to determine the lens mass.

The orbital motion parameters in these models are constrained to ensure consistency with a bound orbit, using the method presented by Muraki et al. (2011). The last column of Table 2 provides the mean and rms of each of the model parameters, and distributions of these parameters are approximately symmetric.

6. Lens Properties

The situation for OGLE-2005-BLG-071 is similar to the case of OGLE-2012-BLG-0950 (Bhattacharya et al. 2018) in that the source radius crossing time, t_*, has not been reliably measured. Fortunately, as discussed above in Section 3.2, it is straight forward to constrain the angular Einstein radius, θ_E,

with our measurement of $\mu_{\rm rel,H}$ given in Equations (1) and (2). The conversion between the heliocentric and geocentric frames only provides a minor complication. This simplest if we assume that the source distance, D_S, is known. In this case, we can determine π_E and $\mu_{\rm rel,G}$ from the measurement of $\mu_{\rm rel,H}$ and light-curve model parameters using Equations (6) and (7). We can then determine the angular Einstein radius from $\theta_E = t_E \mu_{\rm rel,G}$.

Measurements of either angular Einstein radius, θ_E, or the microlensing parallax amplitude, π_E, provide mass–distance relations (Bennett 2008; Gaudi 2012),

$$M_L = \frac{c^2}{4G}\theta_E^2 \frac{D_S D_L}{D_S - D_L} = \frac{c^2}{4G} \frac{\rm au}{\pi_E^2} \frac{D_S - D_L}{D_S D_L},\qquad(9)$$

which can be combined to yield the lens mass in an expression with no dependence on the lens or source distance,

$$M_L = \frac{c^2 \theta_E \,{\rm au}}{4G \pi_E} = \frac{\theta_E}{(8.1439~{\rm mas})\pi_E}M_\odot.\qquad(10)$$
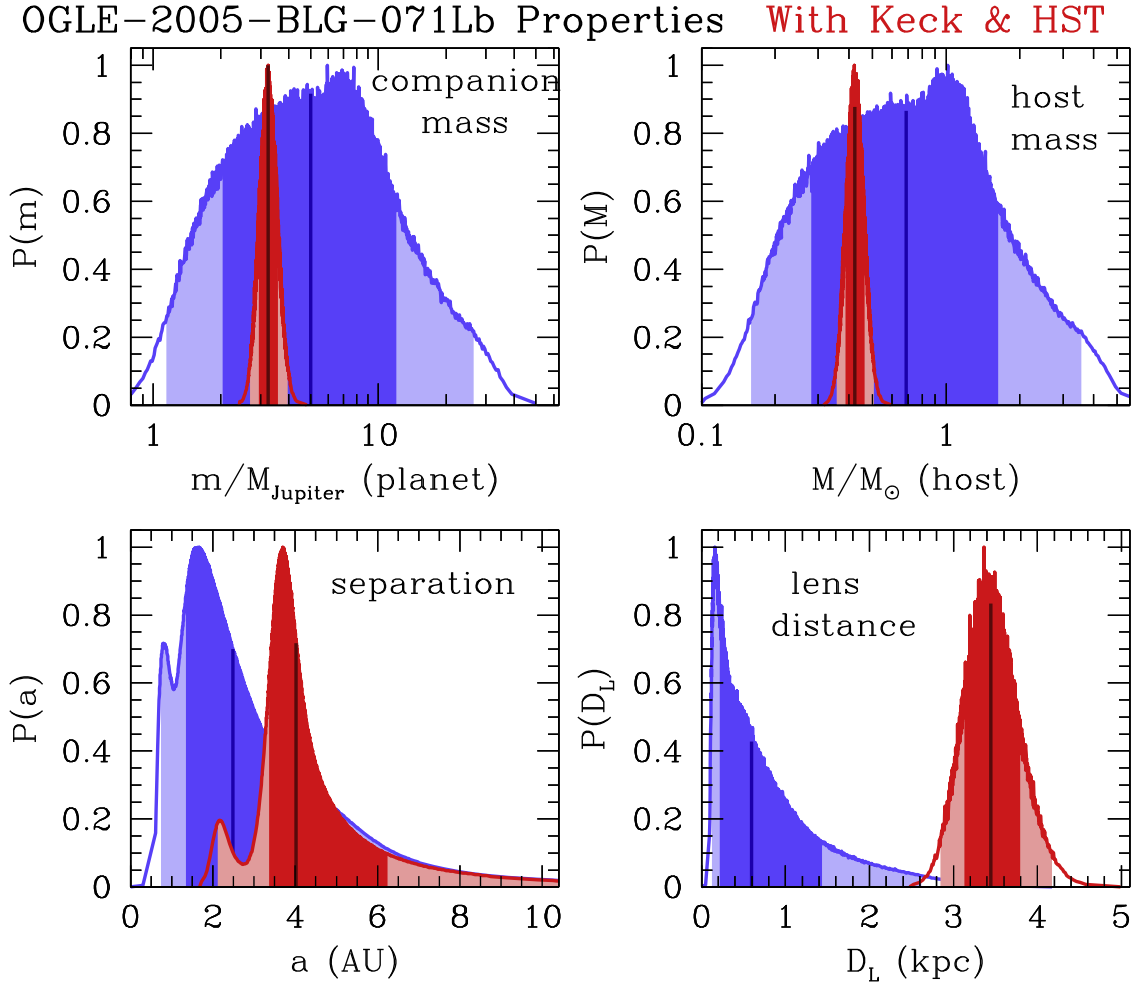
Figure 4. Bayesian posterior probability distributions for the planetary companion mass, host mass, their separation, and the distance to the lens system are shown with only light-curve constraints in blue and with the additional constraints from our Keck and *HST* follow-up observations in red. The central 68.3% of the distributions are shaded in darker colors (dark red and dark blue) and the remaining central 95.4% of the distributions are shaded in lighter colors. The vertical black line marks the median of the probability distribution of the respective parameters.

The lens system distance can also be determined from

$$D_L = \frac{\mathrm{au}}{\pi_E \theta_E + 1/D_S}, \qquad (11)$$

but it does depend on D_S. Our measurement of the host-star K-band magnitude, K_L, also implies a mass–distance relation when combined with our empirical mass–luminosity relation, and the *HST* observations in 2005 and 2006 (Dong et al. 2009b) provide upper limits on the host-star brightness in the I and V bands. As a result, this system is overconstrained with mass measurements from Equation (10) and the combination of Equation (11) and the K-band mass–luminosity relation. In our MCMC light-curve models, we have fixed D_S, and applied χ^2 constraints based on the measured $\mu_{\mathrm{rel,H}}$ and K-band values and the I_L and V_L upper limits.

We follow a somewhat similar procedure in our constrained light-curve modeling. We include both components of π_E and t_* as model parameters even though the light-curve data provide very weak constraints on $\pi_{E,N}$ and t_*. With the π_E and t_* values from each light-curve model, we can determine θ_E and then M_L from Equation (10). With D_S fixed, we use Equation (11) to determine D_L. This provides all the information that we need to determine K_L, I_L, and V_L from

the mass–luminosity relations and Equation (8) and $\mu_{\mathrm{rel,G}}$ from Equation (6). We then calculate addition contributions to χ^2 for each of these five measured parameters (two components of $\mu_{\mathrm{rel,H}}$ and three magnitudes). These χ^2 contributions have the form $\Delta\chi^2 = e^{-(y_{\mathrm{model}}-y_{\mathrm{meas}})^2/2\sigma_y^2}$ where y_{meas} and σ_y measured value and uncertainty, while y_{model} is the model value. The magnitudes are converted to linear fluxes before the constraints are applied, and the V and I constraints are only applied if the model flux is larger than the measured values.

For our final results, we combine the parallel Markov chains for our light-curve models, but we reweight each of the models to remove the fixed distance constraint. We multiply by the inverse of the weighting with the fixed source distance applied in the light-curve model, and then we select a new D_S value from the probability distribution from the Galactic model from Bennett et al. (2014).

Figure 4 and Table 3 provide the results of our analysis. We find that the host star has a mass of $M_{\mathrm{host}} = 0.43 \pm 0.04M_\odot$ and it is orbited by a super-Jupiter mass planet with $m_p = 3.3 \pm 0.3M_{\mathrm{Jup}}$ at a projected separation of $a_\perp = 3.4 \pm 0.5$ au. This translates to a three-dimensional separation of $a_{3d} = 4.0^{+2.3}_{-0.6}$ au under the assumption of a random orientation of the planetary orbit, and the lens system is

Table 3
Measurement of Planetary System Parameters from the Lens Flux Constraints

Parameter	Units	Values and rms	2σ range
Angular Einstein radius, θ_E	mas	0.793 ± 0.042	0.710–0.876
Geocentric lens-source relative proper motion, $\mu_{\rm rel,G}$	mas yr^{-1}	4.25 ± 0.21	3.84–4.66
Host-star mass, $M_{\rm host}$	$M_\odot$	0.426 ± 0.037	0.357–0.506
Planet mass, m_p	$M_{\rm Jup}$	3.27 ± 0.32	2.70–3.96
Host-star–planet 2D separation, $a_\perp$	au	3.38 ± 0.52	1.95–4.08
Host star–planet 3D separation, $a_{\rm 3d}$	au	$4.0^{+2.3}_{-0.6}$	2.1–14.3
Lens distance, D_L	kpc	3.46 ± 0.33	2.85–4.18
Source distance, D_S	**kpc**	9.28 ± 1.17	**6.70–11.14**

located at a distance of $D_L = 3.5 \pm 0.3$ kpc. These distributions are indicated by the red histograms in Figure 4. These results are a dramatic improvement in precision over blue histograms that indicate the parameters predicted by our Bayesian analysis without any constraints from Keck or *HST* observations. However, the lens distance distribution predicted by the unconstrained analysis is peculiar with its sharp peak at very small distances. This is due to the slight light-curve preference for very small source radius crossing time, t_*, values. We suspect that this is due to systematic errors in the Auckland Observatory photometry that were overcome by the much stronger constraints on $\mu_{\rm rel,H}$ and K_L from the Keck images. As discussed by Dong et al. (2009b), the flat-field images from this telescope had serious scattered light problems that were exacerbated by a $180°$ flip of the telescope orientation in the middle of each night. Also, the observations were unfiltered, which led to photometry errors as large as 7% due to differential atmospheric chromatic extinction. It is possible that some of these systematic errors remain after the Dong et al. (2009b) attempts to correct them. For example, their correction for differential chromatic extinction implicitly assumed that the atmospheric chromatic extinction effects remained constant over all four days when the event was at its peak, but the water vapor and aerosol composition of the atmosphere might have changed during that period. This problem was mitigated in the Dong et al. (2009b) analysis by the constraints they placed on the lens brightness and a crude constraint they placed on the lens-source relative proper motion from the color-dependent centroid shift effect (Bennett et al. 2006).

6.1. Comparison to Previous Analysis

Our conclusions are largely in line with those of Dong et al. (2009b), except that we do not have to make the assumption that the unlensed light coincident with the source in the 2005 and 2006 *HST* images is not due to a source companion. While our Keck data are consistent with the existence of a faint source companion, our measurement of the K-band lens brightness indicates that the excess I- and V-band flux seen in the *HST* images is primarily due to the lens star.

The one Dong et al. (2009b) claim that clearly seems to be incorrect is the claim that the OGLE-2005-BLG-071L planetary host star has thick-disk kinematics. Dong et al. (2009b) do not provide many details about how they reach this conclusion, but a primary difference appears to be the fact that they compare their estimated lens velocity to the local standard of rest rather than the kinematics of the Galaxy at the location

of the lens, which was not well understood in 2009 (*Gaia* Collaboration et al. 2018b).

It is also of interest to consider the accuracy of their measurement of the color-dependent centroid shift measurement (Bennett et al. 2006), since this is of interest for the Wide Field Infrared Survey Telescope (WFIRST; Bhattacharya et al. 2018). Dong et al. (2009b) measure offsets between the target (source plus lens blend) centroid in the I- and V-band magnitudes of $\Delta r_{I-V,E} = -0.52 \pm 0.20$ mas and $\Delta r_{I-V,N} = 0.22 \pm 0.20$ mas in the east and north directions, respectively. However, this includes both proper motion and parallax, so to compare to our measurements, we must convert this measurement to the heliocentric reference frame. With our estimate of the lens system distance, D_L, the centroid shift becomes $\Delta r_{I-V,E,H} = -0.45 \pm 0.20$ mas and $\Delta r_{I-V,N,H} = 0.22 \pm 0.20$ mas. We can compare this to the value determined from our precise Keck $\mu_{\rm rel,H}$ measurements. We find $\Delta r_{I-V,E,H} = -0.115 \pm 0.003$ mas and $\Delta r_{I-V,N,H} = 0.100 \pm 0.003$ mas, so the *HST* estimates are off by 1.7σ to the east and 0.5σ to the north. This implies that the Dong et al. (2009b) error bars are consistent with our measurement and that they are not likely to be underestimated by as much as a factor of two.

7. Discussion and Conclusions

Our Keck AO follow-up observations have identified the OGLE-2005-BLG-071L planetary host star through measurements of the lens K-band magnitude and the lens-source relative proper motion, $\mu_{\rm rel,H}$. These measurements allow for the determination of the lens mass and distance through multiple, redundant constraints. The $\mu_{\rm rel,H}$ measurement can be combined with the partial microlensing parallax measurement from the microlensing light curve to yield the lens system masses, and the $\mu_{\rm rel,H}$ measurement can also be combined with the lens K-band magnitude to yield the lens mass and distance, as well. These determinations are consistent with each other, and we combine them to give host and planet masses of $M_{\rm host} = 0.426 \pm 0.037 M_\odot$ and $m_p = 3.27 \pm 0.32 M_{\rm Jup}$, with a projected separation of $a_\perp = 3.38 \pm 0.52$ au at a distance of $D_L = 3.46 \pm 0.33$ kpc. The excess flux seen in the 2005 and 2006 *HST* observations is also consistent with these conclusions.

This confirms that tentative conclusion of Dong et al. (2009b) that this event is a somewhat unexpected sample of a super-Jupiter mass planet orbiting an M dwarf. Such planetary systems are thought to be rare (Laughlin et al. 2004). Since the wide model is slightly favored, the preferred orbital period is 12 yr or more, and this means that many exoplanet Doppler radial velocity surveys do not monitor their stars long enough to detect such planets. However, those surveys that do monitor the radial velocity of low-mass stars for long periods of time claim a low frequency of such planets (Johnson et al. 2010), although they have not yet done a complete statistical analysis. The microlensing statistical analysis of Suzuki et al. (2016, 2018) seems quite consistent with the preliminary radial velocity results since it includes two planets with mass ratios of $q \sim 7 \times 10^{-3}$, when we would expect ~ 700 if there was an average of one such planet orbiting every star. So, we might expect an occurrence rate for such planets of $1/300$ or $1/400$. The other similar planet in the Suzuki et al. (2016) sample is MOA-2008-BLG-379 (Suzuki et al. 2014a, 2014b).

It is expected that the occurrence rate for super-Jupiter planets should be higher for planets that orbit high-metallicity host stars (Fischer & Valenti 2005). Because the host star, OGLE-2005-BLG-071L, can now be resolved from the source star in K-band AO images, it should now be possible to determine the host-star metallicity with moderate resolution K-band spectra (Rojas-Ayala et al. 2010) using instruments such as Keck/OSIRIS and Very Large Telescope/MUSE. Both of these instruments employ AO feeds and OH suppression that are probably required for spectra of sufficient signal-to-noise ratio to measure metallicity.

Finally, we should mention that this event is part of our Keck KSMS program that aims to determine masses and distances for the vast majority of stars in the Suzuki et al. (2016) sample, as well as the MOA 9 yr microlensing event sample that is now under analysis. One important aspect of this program is that it can test an assumption that is currently used to estimate the host mass for most of the planets found by microlensing (Beaulieu et al. 2006; Dong et al. 2009a). For this event, a sub-Saturn mass planet (Bhattacharya et al. 2018) and a Uranus-mass planet (Batista et al. 2015; Bennett et al. 2015), we find that the measured host-star mass is close to the Bayesian prediction, which relies upon the assumption that stars of any mass are equally likely to host the planet with the given mass ratio. This differs from the case of two other targets from our KSMS program: MOA-2007-BLG-400 (A. Bhattacharya et al. 2019, in preparation) and MOA-2013-BLG-220 (Vandorou et al. 2019). The mass measurement for these two events find masses that are at the 94th and 93rd percentile Bayesian analysis prediction based on the equal planet hosting probability assumption. These events also have very similar mass ratios of $q = 2.2 \times 10^{-3}$ and $q = 3.3 \times 10^{-3}$. This suggests that high-mass stars may be much more likely to host planets beyond the snow line with mass ratios in the $0.002 < q < 0.0035$ range, but our OGLE-2005-BLG-071 result suggests that this trend may not hold at higher mass ratios. Clearly, more mass microlens exoplanet host-star mass measurements are needed to confirm such speculation.

ORCID iDs

David P. Bennett https://orcid.org/0000-0001-8043-8413

Jean-Philippe Beaulieu https://orcid.org/0000-0003-0014-3354
Joshua W. Blackman https://orcid.org/0000-0001-5860-1157
Aikaterini Vandorou https://orcid.org/0000-0002-9881-4760
Sean K. Terry https://orcid.org/0000-0002-5029-3257
Andrew A. Cole https://orcid.org/0000-0003-0303-3855
Naoki Koshimoto https://orcid.org/0000-0003-2302-9562
Jessica R. Lu https://orcid.org/0000-0001-9611-0009
Clément Ranc https://orcid.org/0000-0003-2388-4534

References

Anderson, J., & King, I. R. 2000, PASP, 112, 1360
Anderson, J., & King, I. R. 2004, Multi-filter PSFs and Distortion Corrections for the HRC, Instrument Science Report ACS 2004-15
Anderson, J., & King, I. R. 2006, PSFs, Photometry, and Astronomy for the ACS/WFC, Instrument Science Report ACS 2006-01
Anglada-Escudé, G., Boss, A. P., Weinberger, A. J., et al. 2012, ApJ, 746, 37
Batista, V., Beaulieu, J.-P., Bennett, D. P., et al. 2015, ApJ, 808, 170
Batista, V., Beaulieu, J.-P., Gould, A., et al. 2014, ApJ, 780, 54
Batista, V., Gould, A., Dieters, S., et al. 2011, A&A, 529, A102
Beaulieu, J.-P., Batista, V., Bennett, D. P., et al. 2018, AJ, 155, 78
Beaulieu, J.-P., Bennett, D. P., Batista, V., et al. 2016, ApJ, 824, 83
Beaulieu, J.-P., Bennett, D. P., Fouqué, P., et al. 2006, Natur, 439, 437
Bennett, D. P. 2008, in Exoplanets, ed. J. W. Mason (Berlin: Springer), 47
Bennett, D. P. 2010, ApJ, 716, 1408
Bennett, D. P., Anderson, J., Bond, I. A., Udalski, A., & Gould, A. 2006, ApJL, 647, L171
Bennett, D. P., Anderson, J., & Gaudi, B. S. 2007, ApJ, 660, 781
Bennett, D. P., Batista, V., Bond, I. A., et al. 2014, ApJ, 785, 155
Bennett, D. P., Bhattacharya, A., Anderson, J., et al. 2015, ApJ, 808, 169
Bennett, D. P., Bond, I. A., Abe, F., et al. 2017, AJ, 154, 68
Bennett, D. P., Rhie, S. H., Nikolaev, S., et al. 2010, ApJ, 713, 837
Bennett, D. P., Udalski, A., Bond, I. A., et al. 2018, AJ, 156, 113
Bertin, E. 2010a, SCAMP: Automatic Astrometric and Photometric Calibration, Astrophysics Source Code Library, ascl:1010.063
Bertin, E. 2010b, SWarp: Resampling and Co-adding FITS Images Together, Astrophysics Source Code Library, ascl:1010.068
Bertin, E., & Arnouts, S. 1996, A&AS, 117, 393
Bertin, E., Delorme, P., & Bouy, H. 2012, ASSP, 29, 71
Bertin, E., Mellier, Y., Radovich, M., et al. 2002, in ASP Conf. Ser. 281, Astronomical Data Analysis Software and Systems XI, ed. D. A. Bohlender, D. Durand, & T. H. Handley (San Francisco, CA: ASP), 228
Bhattacharya, A., Beaulieu, J.-P., Bennett, D. P., et al. 2018, AJ, 156, 289
Carpenter, J. M. 2001, AJ, 121, 2851
Delfosse, X., Forveille, T., Ségransan, D., et al. 2000, A&A, 364, 217
Dolphin, A. E. 2000, PASP, 112, 1383
Dong, S., Bond, I. A., Gould, A., et al. 2009a, ApJ, 698, 1826
Dong, S., Gould, A., Udalski, A., et al. 2009b, ApJ, 695, 970
Fischer, D. A., & Valenti, J. 2005, ApJ, 622, 1102
Gaia Collaboration, Brown, A. G. A., Vallenari, A., et al. 2018a, A&A, 616, A1
Gaia Collaboration, Katz, D., Antoja, T., et al. 2018b, A&A, 616, A11
Gaudi, B. S. 2012, ARA&A, 50, 411
Gaudi, B. S., Bennett, D. P., Udalski, A., et al. 2008, Sci, 319, 927
Ghosh, H., DePoy, D. L., Gal-Yam, A., et al. 2004, ApJ, 615, 450
Gonzalez, O. A., Rejkuba, M., Zoccali, M., Valenti, E., & Minniti, D. 2011, A&A, 534, A3
Gould, A. 2014, JKAS, 47, 215
Gould, A., Miralda-Escude, J., & Bahcall, J. N. 1994, ApJL, 423, L105
Gubler, J., & Tytler, D. 1998, PASP, 110, 738
Han, C., Bennett, D. P., Udalski, A., et al. 2019, AJ, 158, 114
Henry, T. J., Franz, O. G., Wasserman, L. H., et al. 1999, ApJ, 512, 864
Henry, T. J., & McCarthy, D. W., Jr. 1993, AJ, 106, 773
Hirao, Y., Udalski, A., Sumi, T., et al. 2017, AJ, 154, 1
Johnson, J. A., Aller, K. M., Howard, A. W., & Crepp, J. R. 2010, PASP, 122, 905
Johnson, J. A., Butler, R. P., Marcy, G. W., et al. 2007, ApJ, 670, 833
Jung, Y. K., Udalski, A., Sumi, T., et al. 2015, ApJ, 798, 123
Kennedy, G. M., & Kenyon, S. J. 2008, ApJ, 673, 502
Kenyon, S. J., & Hartmann, L. 1995, ApJS, 101, 117

King, I. R. 1983, PASP, 95, 163
Koshimoto, N., Shvartzvald, Y., Bennett, D. P., et al. 2017, AJ, 154, 3
Koshimoto, N., Udalski, A., Sumi, T., et al. 2014, ApJ, 788, 128
Laughlin, G., Bodenheimer, P., & Adams, F. C. 2004, ApJL, 612, L73
Lindegren, L. 2018, Re-normalising the Astrometric Chi-square in Gaia DR2, Tech. Note, GAIA-C3-TN-LU-LL-124-01, Lund Observatory
Minniti, D., Lucas, P. W., Emerson, J. P., et al. 2010, NewA, 15, 433
Muraki, Y., Han, C., Bennett, D. P., et al. 2011, ApJ, 741, 22
Nataf, D. M., Gould, A., Fouqué, P., et al. 2013, ApJ, 769, 88
Nishiyama, S., Tamura, M., Hatano, H., et al. 2009, ApJ, 696, 1407
Poleski, R., Udalski, A., Bond, I. A., et al. 2017, A&A, 604, A103
Poleski, R., Udalski, A., Dong, S., et al. 2014, ApJ, 782, 47
Rhie, S. H., Becker, A. C., Bennett, D. P., et al. 1999, ApJ, 522, 1037
Rojas-Ayala, B., Covey, K. R., Muirhead, P. S., & Lloyd, J. P. 2010, ApJL, 720, L113
Service, M., Lu, J. R., Campbell, R., et al. 2016, PASP, 128, 095004

Shin, I.-G., Ryu, Y.-H., Udalski, A., et al. 2016, JKAS, 49, 73
Shin, I.-G., Ryu, Y.-H., Yee, J. C., et al. 2019, AJ, 157, 146
Shvartzvald, Y., Maoz, D., Kaspi, S., et al. 2014, MNRAS, 439, 604
Stetson, P. B. 1987, PASP, 99, 191S
Street, R. A., Choi, J.-Y., Tsapras, Y., et al. 2013, ApJ, 763, 67
Suzuki, D., Bennett, D. P., Ida, S., et al. 2018, ApJL, 869, L34
Suzuki, D., Bennett, D. P., Sumi, T., et al. 2016, ApJ, 833, 145
Suzuki, D., Udalski, A., Sumi, T., et al. 2014a, ApJ, 780, 123
Suzuki, D., Udalski, A., Sumi, T., et al. 2014b, ApJ, 788, 97
Szymański, M. K., Udalski, A., Soszyński, I., et al. 2011, AcA, 61, 83
Tsapras, Y., Choi, J.-Y., Street, R. A., et al. 2014, ApJ, 782, 48
Udalski, A., Jaroszyński, M., Paczyński, B., et al. 2005, ApJL, 628, L109
Vandorou, A., Bennett, D. P., Beaulieu, J.-P., et al. 2019, arXiv:1909.04444
Yelda, S., Lu, J. R., Ghez, A. M., et al. 2010, ApJ, 725, 331
Zang, W., Hwang, K.-H., Kim, H.-W., et al. 2018, AJ, 156, 236